

Minute-scale gravimetry using a coherent atomic spatial superposition

Authors: Cristian D. Panda^{*1}, Matt Tao¹, James Egelhoff¹, Miguel Ceja¹, Victoria Xu^{1†}, Holger Müller^{*1}

¹Department of Physics, University of California, Berkeley, 94720, CA, USA.

^{*}Corresponding authors. Email: cpanda@berkeley.edu, hm@berkeley.edu

Abstract: In quantum metrology and quantum information processing, a coherent nonclassical state must be manipulated before unwanted interactions with the environment lead to decoherence. In atom interferometry, the nonclassical state is a spatial superposition, where each atom coexists in multiple locations as a collection of phase-coherent partial wavepackets. These states enable precise measurements in fundamental physics and inertial sensing. However, atom interferometers usually use atomic fountains, where the available interrogation time is limited to ~ 3 seconds (for 10 m fountains). Here, we analyze the theoretical and experimental limits to the coherence arising from collective dephasing of the atomic ensemble and realize atom interferometry with a spatial superposition state that is maintained for as long as 70 seconds. These gains in coherence may enable gravimetry measurements, searches for fifth forces, or fundamental probes into the non-classical nature of gravity.

[†] Present address: Massachusetts Institute of Technology, Cambridge, MA 02139, USA

Nonclassical states whose coherence can be maintained for tens of seconds or even minutes are at the forefront of quantum science. For example, optical lattice clocks with atoms trapped for 15 seconds have enabled 2-3 orders of magnitude gains^{1,2} in precision relative to atomic fountain clocks. In atom interferometry, achieving minute-scale coherence times would be instrumental for portable and vibration insensitive gravimetry³⁻⁵ and many applications that are currently out of reach, such as testing the quantum nature of gravity^{6,7}, or increasingly precise searches of dark energy candidates^{8,9}. However, atomic fountains have been limited to 2.3 seconds by the free-fall times available in 10-meter fountains¹⁰. Since the height required scales quadratically with time, experiments with fountains measuring hundreds of meters¹¹⁻¹⁴, sounding rockets^{15,16}, zero-gravity planes¹⁷, drop towers¹⁸, and in microgravity on the International Space Station^{19,20} aim for several seconds of interrogation time, but none are currently proposed to achieve minute-scale coherence.

Initial attempts to trap atoms in an optical lattice have suffered from dephasing in the trap, limiting coherence to 1 second²¹⁻²³. Recently, we used the mode of a Fabry-Perot cavity to strongly reduce optical lattice imperfections, extending measurement time to 20 seconds²⁴. However, the exact fundamental or technical limits remained unexplored, limiting achieved coherence.

Here, we elucidate these limits, observing coherences for as long as 70 seconds, the longest-lasting spatial superposition of any massive particles, 30 times longer than possible with atoms in free-fall¹⁰. Compared to atomic fountains, the mm-scale trajectories in our experiment facilitate maintaining homogeneity of electric, magnetic, and gravitational fields at levels required for precision measurement²⁵. We experimentally investigate the sources of decoherence, identify key influences, and develop a framework to describe decoherence in the optical lattice.

A coherent quantum spatial superposition state held by an optical lattice for 70 seconds

The experiment sequence starts by preparing a sample of cold Cesium (Cs-133) atoms (**Figure 1a**) in the magnetically insensitive $m_F = 0$ state of the ground hyperfine manifold of the Cesium atom (see Supplementary Materials). The atoms are launched upwards by a moving optical lattice (**Figure 1b**) and their axial temperature is further reduced by a Fourier-limited Raman π -pulse to 80 nK. In free fall, counterpropagating laser pulses at 852 nm wavelength stimulate two-photon Raman transitions between the $F = 3$ and $F = 4$ hyperfine ground states²⁶. These pulses' intensities and durations are tuned to transfer atoms with a 50% probability ($\pi/2$ pulses). This leads to a coherent beam splitter that separates the atomic matter-wave into two partial wavepackets that move with a differential velocity of $2v_r = \hbar k_{\text{eff}}/m_{\text{Cs}} = 7 \text{ mm/s}$ given by the momentum of the 852 nm photons, where k_{eff} is the laser field wavevector and m_{Cs} is the Cs atom mass.

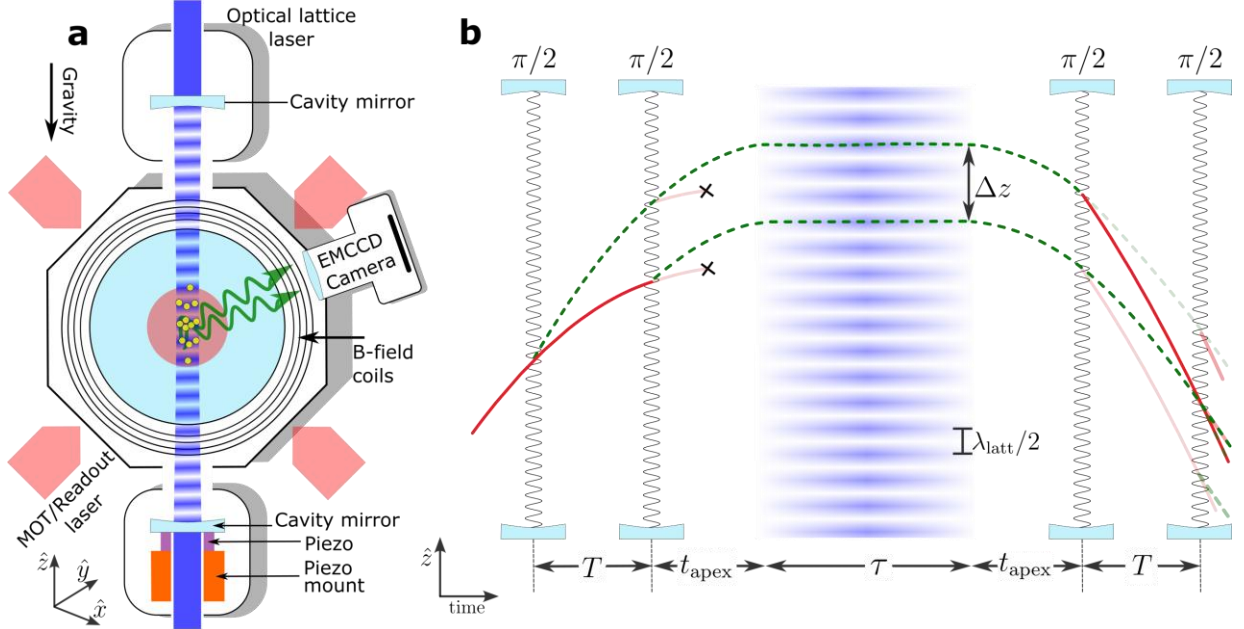


Figure 1. a, Schematic of the apparatus. Cs atoms (small yellow disks) are magneto-optically trapped (MOT) at the center of an ultra-high vacuum chamber by 6 laser beams (red, wavelength 852 nm, near resonant with the Cs D2-line). They are loaded into the high-intensity regions of the standing wave of an optical lattice laser (dark blue, wavelength 943 nm), formed by the fundamental mode of a vertically oriented Fabry-Perot cavity (mirrors in light blue). A ring piezo (purple) keeps the cavity length constant. **b**, Atom interferometer trajectories. Pairs of $\pi/2$ pulses (wavy vertical lines) separated by time T split, redirect and interfere the launched atomic wavepacket. At the apex of their free-fall trajectory, the atoms are loaded in the far-detuned optical lattice (horizontal blue stripes) where they remain for time τ . The internal atomic state of each interferometer arm is either $F = 3$ (red, solid lines) or $F = 4$ (green, dashed lines) hyperfine levels.

Applying a pair of $\pi/2$ pulses, separated by a time T , splits the matter-waves four-fold. We select two wavepackets that are moving at a constant separation $\Delta z = 2v_r T$, while sharing the same internal quantum state and external momentum. When they reach the apex, they are loaded into the high-intensity regions of a far-detuned optical lattice with a spatial periodicity of $\lambda_{\text{latt}}/2$, where $\lambda_{\text{latt}} = 943$ nm is the wavelength of the lattice laser. After a hold time τ , they are adiabatically unloaded and recombined using a final pair of $\pi/2$ pulses.

Due to the resulting interference, the phase difference $\Delta\phi = \phi_t - \phi_b$ accumulated between the top and bottom wavepackets determines the probabilities $P_{3,4} = [1 \pm C \cos(\Delta\phi)]/2$ of detecting an atom in the output ports corresponding to $F=3$ and $F=4$, where C is the fringe contrast. The maximum contrast is $C = 0.5$ because only two of the four interferometer outputs interfere. The atom numbers ($N_{3,4}$) in each port, which are proportional to $P_{3,4}$, are measured through fluorescence imaging. We extract the interferometer phase, $\Delta\phi$, from the measured population asymmetry, $A = \frac{N_3 - N_4}{N_3 + N_4} = C \cos(\Delta\phi)$. The primary contribution to interferometer phase is the propagation phase $\Delta\phi_{\text{grav}}^{\text{prop}}$ (see Supplementary Materials for other contributions), which accumulates due to the gravitational potential difference $\Delta U_{\text{grav}} = m_{\text{Cs}} g \Delta z$ between the top and bottom interferometer arms during the lattice hold and is obtained by integrating the Lagrangian \mathcal{L} over the classical trajectory²⁷,

$$\Delta\phi_{\text{grav}}^{\text{prop}} = \frac{1}{\hbar} \left(\int_{t=0}^{\tau} \mathcal{L}^t dt - \int_{t=0}^{\tau} \mathcal{L}^b dt \right) = \frac{1}{\hbar} \int_{t=0}^{\tau} \Delta U dt = \frac{m_{\text{Cs}} g \Delta z}{\hbar} \tau. \quad (1)$$

The apparatus contains several upgrades over our previous one²⁴. Improved sample preparation and a more efficient moving-lattice launch cumulatively increased atom number 40-fold. Lower atomic sample temperature provided 1.4-fold contrast. A further detuned optical lattice laser (943 nm instead of 866 nm) reduced decoherence from single photon-scattering. Improved stabilization of the intra-cavity lattice laser intensity increased the atomic lifetime to 14 seconds from 7 seconds. Imaging efficiency was improved through reduction of stray light using blackened radiation shields and the use of an electron-multiplied charge-coupled devices (EMCCD) camera with high ($\sim 40\%$ at 852 nm) quantum efficiency and low noise. Laser phase noise has been reduced by a more stable radio frequency (rf) reference.

As a result, the interferometer precision is now consistent with the standard quantum limit over the entire range of wavepacket separations, hold time, and trap depths explored in this paper. This means that further signal and coherence upgrades are very likely to convert to sensitivity gains.

In addition, we now observe up to 70 seconds of coherent phase accumulation across the atomic spatial superposition state (**Figure 2**). This interferometer used a pulse separation $T = 0.267$ ms ($\Delta z = 1.9 \mu\text{m}$) and a peak trap depth of $U_0 = 7 E_r$. We use the Cs atom recoil energy at 852 nm, $E_r = m_{\text{Cs}} v_r^2 / 2 = \hbar \cdot 2\pi \cdot 2.0663 \text{ kHz}$ as a unit of energy, even though the lattice wavelength is 943 nm.

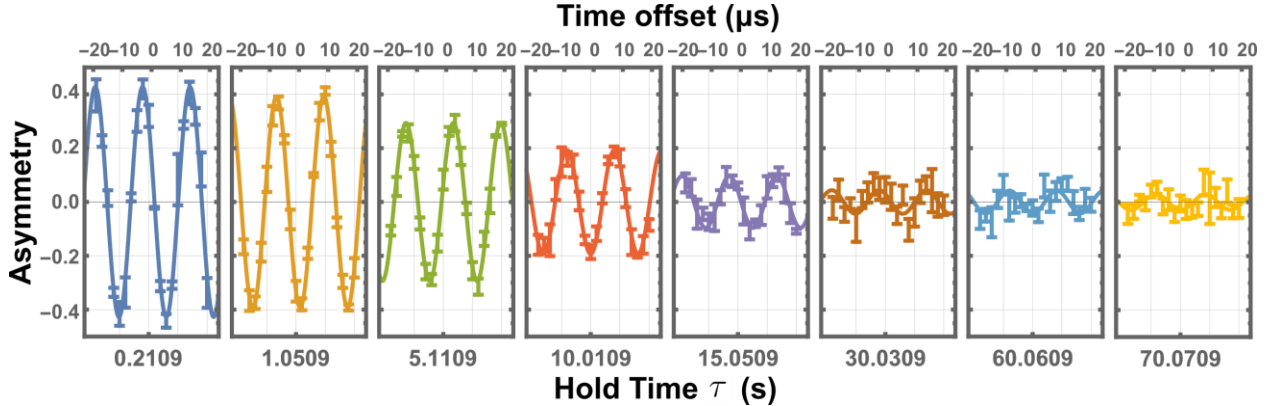


Figure 2. Interference fringes with over one minute coherence. Oscillations in the asymmetry are shown as the interferometer phase varies proportionally to the hold time τ . Each datapoint corresponds to the average of a few experiment cycles. The error bars correspond to 1σ standard error. Fringe offsets are removed.

Measured lattice decoherence

We quantify interferometer coherence by extracting the fringe contrast, C , from a least-squares fit of the interferometer fringes with contrast, phase, and fringe offset as free parameters. For hold times $\tau < 20$ s, we observe the contrast to decay exponentially with the hold-time, τ : $C = C_0 \text{Exp}(-\tau/\tau_c)$ (**Figure 3a**), where C_0 is the interferometer contrast with no hold time ($C_0 \sim 0.5$ typically).

The decay time constant τ_c is measured to be inversely proportional to the atomic wavepacket separation, Δz , and the trap depth, U_0 (**Figure 3b**)

$$1/\tau_c = U_0 \Delta z / \kappa. \quad (2)$$

Here, $\kappa = 110 \mu\text{m} \cdot \text{s} \cdot E_r$ is the measured global contrast decay constant. Holding the atoms against Earth's gravitational field requires $U_0 > 4 E_r$ (experimentally measured) for trap lifetimes exceeding 10 s. We used a trap depth of $7 E_r$ above (**Figure 2**), sufficient to detect several hundred

atoms per 70 second experiment cycle. Operation in microgravity¹⁹ would allow a strong reduction in the trap depth. We note that beyond $\tau = 20$ s, the contrast is observed to decay more slowly, consistent with our model (see below and Supplementary Materials).

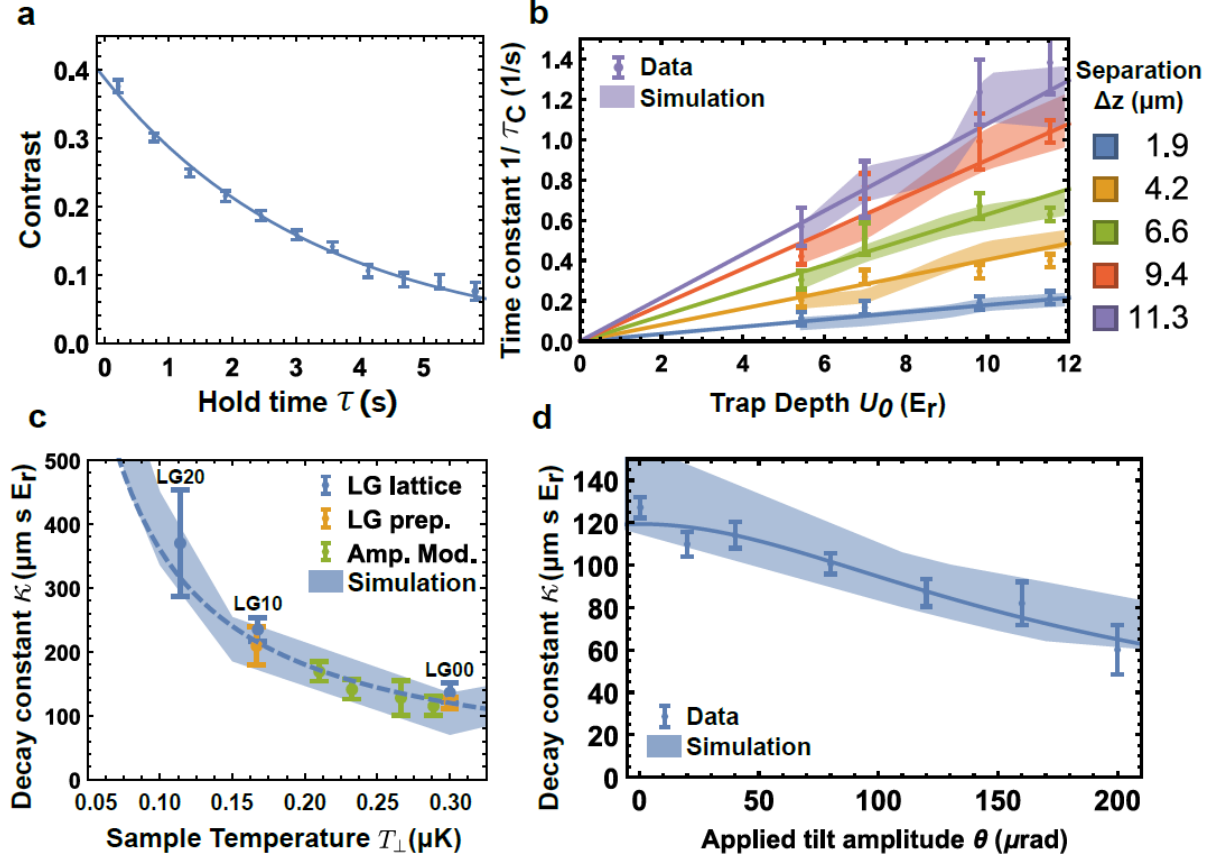


Figure 3. Decoherence during optical lattice hold. **a**, Contrast decays exponentially vs hold time τ with time constant τ_C , $C = C_0 \text{Exp}[-\tau/\tau_C]$. **b**, τ_C is inversely proportional to wavepacket separation, Δz , and trap depth, U_0 : $1/\tau_C = U_0 \Delta z \kappa$. **c**, The global contrast decay constant κ increases when using atomic ensembles that are colder transversally. The dashed line shows $\kappa(T_{\perp}) = \kappa_0 * T_{\perp}^0/T_{\perp}$. **d**, Decrease of the contrast decay constant κ with magnitude of applied tilt θ_{app} . The line is a fit to equation $\kappa(\theta_{\text{app}}) = \kappa_0 / \sqrt{1 + (\theta_{\text{app}}/\theta_0)^2}$. All data points are shown with error bars corresponding to 1σ standard error. The color bands correspond to 1σ (68%) Gaussian confidence bands determined by the statistical uncertainty of a numerical simulation that estimates atomic ensemble dephasing in the presence of residual atomic motion and lattice tilt noise.

To understand the physical mechanisms that limit the coherence time, we tested many modifications to the experiment. We found that κ was robust against several strong changes to the setup. This includes using higher-quality cavity mirrors (surface rms roughness < 1 Å) as opposed to standard dielectric mirrors as well as locating the cavity waist near the atoms, so that lattice potential is unchanged between the two interferometer arms. We also found that lattice laser imperfections (frequency noise, broadband emission, background scatter, imperfect cavity coupling), alignment of the lattice with gravity, atom density and axial temperature (which is much lower than the transversal temperature due to axial velocity selection), properties of the lattice laser beam (polarization, wavelength), symmetry of interferometry pulses and magnetic fields (see Supplementary Materials for details), did affect κ .

However, κ is improved up to 3-fold when using higher order Laguerre-Gaussian (LG) modes for the optical lattice hold (**Figure 3c**). One possible explanation is that loading into higher-order

cavity modes selects a subset of atoms with a lower transverse temperature, T_{\perp} . The radially symmetric LG10 and LG20 modes have a central intensity peak that is narrower than the fundamental LG00 Gaussian mode (widths of 56% and 43% respectively at half maximum). The selection occurs when the narrower lattice beam captures only atoms near the center of the atom cloud. (The low intensity “rings” of the higher-order modes are too weak to trap atoms and have poor overlap with the atom sample, so atoms only get trapped in the central peaks.) We corroborate this interpretation by temperature measurements of the trapped atoms using time-of-flight (TOF) spectroscopy to be coldest (Fig. 3c). We believe that the reason for the lower temperature is twofold: first, a spatial variation of the intensity of cavity-derived Raman-sideband cooling beams, and second, that the fastest-moving atoms disappear from the trapping region in the 38 ms interval between laser cooling and lattice loading.

To further corroborate that the lower transverse temperature is the cause for improved coherence, we have used the LG10 mode to temperature-select the atomic sample while switching back to the LG00 fundamental mode during interferometry hold. A TOF measurement confirms that the LG10 mode selects an atom sample that is 1.8 times colder. We observe a 1.8-fold increase in the contrast decay constant κ (**Figure 3c**).

We further confirm that coherence depends on sample temperature by “boiling off” the most energetic atoms by amplitude-modulating the lattice during the initial 500 ms of the hold. The lattice trap depth was set to $U_0 = 14 E_r$, corresponding to axial trap frequency $\omega = 2\pi \cdot 14$ kHz. The modulation has an amplitude of 5% of the trap depth at a frequency that is twice the trap frequency. This reduces the sample temperature to 70% of the initial value, as measured through TOF. We observe that this reduces the number of remaining atoms 3-fold and leads to an increase in contrast (**Figure 3c**).

In addition to the atom temperature, we observe that oscillatory tilts $\theta(t)$ of the trapping laser beam with respect to the vertical are a strong influence on κ . To demonstrate this, we shake the experiment (which is floating on minus-K vibration isolators) along the $-\hat{x}$ axis (Fig. 1) using a voice coil, typically at $2\pi \cdot 600$ Hz. The resulting tilt amplitude θ_{app} was quantified by measuring the position of the cavity transmitted laser beam on a quadrant photodetector. Fringes were measured for varying amplitudes of applied tilt (**Figure 3d**). The resulting κ was fitted to a model $\kappa(\theta_{\text{app}}) = \kappa_0 / (1 + (\theta_{\text{app}}/\theta_0)^2)^{1/2}$, where θ_{app} is the applied tilt and the fitted $\theta_0 = 120 \mu\text{rad}$ is the residual environmental tilt.

We independently quantify the environmental tilt spectrum in our experiment θ_0 . The spectrum consists of multiple peaks, with the largest components in the few hundred hertz band, with a total rms tilt of $200 \pm 150 \mu\text{rad}$, consistent with that obtained from the fit above.

Understanding decoherence due to atomic ensemble dephasing

The above observations are compatible with a model that connects the global contrast decay constant κ with time-dependent tilts and residual atomic motion. This framework can also be used in general to quantify decoherence due to many other experimental imperfections.

In addition to the gravitational phase difference $\Delta\phi_{\text{grav}}^{\text{prop}}$ (Eq. 1), each arm of the interferometer accumulates phase due to the lattice lightshift (AC Stark shift) from the optical potential U_{latt} . U_{latt} has a Gaussian profile in the transverse xy -plane and depends sinusoidally on z : $U_{\text{latt}} =$

$U_0 \text{Exp}\left(-\frac{x^2+y^2}{2w_0^2}\right) \text{Sin}^2\left(\frac{2\pi z}{\lambda_{\text{latt}}}\right)$, where $w_0 \approx 760 \mu\text{m}$ is the radius of the cavity mode. For an atom at rest at the center of a lattice with $U_0 = 7 E_r$, $\phi_{\text{latt}}^{\text{prop}} = 6.4 \text{ Mrad}$ after $\tau = 70$ seconds.

Ideally, the trapping potentials for the top and bottom interferometer arms are identical, so that $\Delta\phi_{\text{latt}}^{\text{prop}} = \phi_{\text{latt}}^t - \phi_{\text{latt}}^b \cong 0$. However, any difference in the optical potential between the top and bottom arms, $\Delta U_{\text{latt}} = U^t - U^b$, will lead to a differential phase shift $\Delta\phi_{\text{latt}}^{\text{prop}} \propto \Delta U_{\text{latt}} \neq 0$. In addition, ΔU_{latt} moves the top and bottom partial wave packets relative to each other, so that they do not overlap exactly at the end of the interferometer. This leads to a separation phase $\Delta\phi_{\text{latt}}^{\text{sep}} = \sum_{i=\{x,y\}}(i^t - i^b)(v_i^t + v_i^b)m_{\text{Cs}}/(2\hbar)^{28}$. The lattice phase shift is thus given by $\Delta\phi_{\text{latt}} = \Delta\phi_{\text{latt}}^{\text{prop}} + \Delta\phi_{\text{latt}}^{\text{sep}}$.

Despite taking great care to minimize experimental imperfections, as described above, sources of differential phase shift remain. In particular, time-dependent tilts due to vibrations cause the top and bottom lattice sites to oscillate transversally with a differential amplitude proportional to Δz : $a_{\text{tilt}}(t) = \theta(t) \cdot \Delta z$. This motion causes a differential potential, $\Delta U_{\text{tilt}}(t) \propto \Delta z \cdot \theta(t) \cdot U_{\text{latt}}^0$. To first order, the equations above give a linear phase shift as a function of tilt amplitude, trap depth, separation and hold time

$$\Delta\phi_{\text{latt}}^{\text{tilt}} \propto \Delta z \cdot \theta(t) \cdot U_{\text{latt}}^0 \tau. \quad (3)$$

The lattice phase shift also depends on the distribution of atomic trajectories in the ensemble, which motivates the transverse temperature dependence observed above. We focus here on motion in the transverse xy -plane, where the atoms follow orbital motion around the center of the optical trap. These trajectories can be treated semi-classically. A representative atomic-motion timescale is given by the transverse harmonic trap frequency $\omega_{\perp} = 2\pi \cdot 2.8 \text{ Hz}$, much slower than the measured cavity tilts which typically occur at frequencies $> 2\pi \cdot 100 \text{ Hz}$. However, the trajectories have appreciable non-harmonic components, because of the long tails of the Gaussian potential. The spread in initial velocities and positions causes the lattice phase to accumulate at different rates for different atoms. This means that a hotter atom cloud has a wider phase dispersion

$$\delta(\Delta\phi_{\text{latt}}) \propto \Delta z \cdot \theta(t) \cdot U_{\text{latt}}^0 \tau T_{\perp}. \quad (4)$$

We simulate the atomic trajectories numerically to estimate the proportionality factors (see Supplementary Materials). The simulations result in a Lorentzian phase distribution across the sample, $P(\Delta\phi) = \frac{1}{\pi} \cdot \frac{\delta(\Delta\phi_{\text{latt}})}{\Delta\phi^2 + [\delta(\Delta\phi_{\text{latt}})]^2}$, with a width $\delta(\Delta\phi_{\text{latt}})$ that scales like Eq. (4). We use a density matrix formalism (see Supplementary Material) to show that this Lorentzian phase distribution results in an exponential decay of the ensemble contrast²⁹ with $\delta(\Delta\phi_{\text{latt}})$

$$C = C_0 \exp[-\delta(\Delta\phi_{\text{latt}})]. \quad (5)$$

Thus, the combination of differential phase shift due to tilts (Eq. (3)), phase dispersion due to residual atomic motion (Eq. (4)) and ensemble collective dephasing (Eq. (5)) predicts a decoherence model

$$C = C_0 \exp[-\Delta z \cdot U_{\text{latt}}^0 \cdot \tau / \kappa], \quad (6)$$

where $\kappa \propto (\theta(t) T_{\perp})^{-1}$. The contrast decay model predictions are quantified through numerical simulation, which results in quantitative agreement to the experimental data (**Figure 3**).

Discussion

In conclusion, we have demonstrated the longest-lasting spatial superposition state of a massive particle to date by measuring interference of atomic Cesium wavepackets after 70 seconds of hold time. We explain the measured decoherence as resulting from residual atomic motion causing the spatial superposition state to differentially sample optical trap imperfections due to tilt.

Our models and experimental tests suggest further improvement in atom numbers and readout noise, reduction of atom sample temperature and reduction of oscillatory tilts may lead to spatial superposition states with ultra-long coherence, exceeding minutes. These increases in coherence are landmark results towards applications such as gravimetry^{3–5}, searches for fifth forces^{8,9}, or fundamental probes into the non-classical nature of gravity^{6,7,30}.

1. Marti, G. E. *et al.* Imaging Optical Frequencies with 100 μHz Precision and 1.1 μm Resolution. *Phys Rev Lett* **120**, (2018).
2. Ohmae, N. *et al.* Transportable Strontium Optical Lattice Clocks Operated Outside Laboratory at the Level of 10–18 Uncertainty. *Adv Quantum Technol* **4**, (2021).
3. van Camp, M. *et al.* Geophysics From Terrestrial Time-Variable Gravity Measurements. *Reviews of Geophysics* vol. 55 938–992 Preprint at <https://doi.org/10.1002/2017RG000566> (2017).
4. Hu, Z. K. *et al.* Demonstration of an ultrahigh-sensitivity atom-interferometry absolute gravimeter. *Phys Rev A* **88**, (2013).
5. Wu, X. *et al.* Gravity surveys using a mobile atom interferometer. *Sci. Adv* **5**, 800–806 (2019).
6. Carney, D., Müller, H. & Taylor, J. M. Using an atom interferometer to infer gravitational entanglement generation. *PRX Quantum* **2**, (2021).
7. Hohensee, M. A., Estey, B., Hamilton, P., Zeilinger, A. & Müller, H. Force-free gravitational redshift: Proposed gravitational Aharonov-Bohm experiment. *Phys Rev Lett* **108**, (2012).
8. Jaffe, M. *et al.* Testing sub-gravitational forces on atoms from a miniature in-vacuum source mass. *Nat Phys* **13**, 938–942 (2017).
9. Sabulsky, D. O. *et al.* Experiment to Detect Dark Energy Forces Using Atom Interferometry. *Phys Rev Lett* **123**, (2019).
10. Dickerson, S. M., Hogan, J. M., Sugarbaker, A., Johnson, D. M. S. & Kasevich, M. A. Multiaxis inertial sensing with long-time point source atom interferometry. *Phys Rev Lett* **111**, (2013).
11. Yijun Jiang *et al.* Matter-wave Atomic Gradiometer Interferometric Sensor (MAGIS-100). *Quantum Sci Technol* **6**, (2021).
12. Badurina, L. *et al.* AION: An atom interferometer observatory and network. *Journal of Cosmology and Astroparticle Physics* **2020**, (2020).
13. Canuel, B. *et al.* Exploring gravity with the MIGA large scale atom interferometer. *Sci Rep* **8**, (2018).
14. Zhan, M. S. *et al.* ZAIGA: Zhaoshan long-baseline atom interferometer gravitation antenna. *International Journal of Modern Physics D* **29**, (2020).
15. Becker, D. *et al.* Space-borne Bose–Einstein condensation for precision interferometry. *Nature* **562**, 391–395 (2018).
16. Lachmann, M. D. *et al.* Ultracold atom interferometry in space. *Nat Commun* **12**, (2021).
17. Barrett, B. *et al.* Dual matter-wave inertial sensors in weightlessness. *Nat Commun* **7**, (2016).
18. Deppner, C. *et al.* Collective-Mode Enhanced Matter-Wave Optics. *Phys Rev Lett* **127**, (2021).
19. Aveline, D. C. *et al.* Observation of Bose–Einstein condensates in an Earth-orbiting research lab. *Nature* **582**, 193–197 (2020).
20. Frye, K. *et al.* The Bose-Einstein Condensate and Cold Atom Laboratory. *EPJ Quantum Technol* **8**, (2021).
21. Cladé, P. *et al.* A promising method for the measurement of the local acceleration of gravity using Bloch oscillations of ultracold atoms in a vertical standing wave. *Europhys Lett* **71**, 730–736 (2005).
22. Zhang, X., del Aguila, R. P., Mazzoni, T., Poli, N. & Tino, G. M. Trapped-atom interferometer with ultracold Sr atoms. *Phys Rev A* **94**, (2016).
23. Charrière, R., Cadoret, M., Zahzam, N., Bidet, Y. & Bresson, A. Local gravity measurement with the combination of atom interferometry and Bloch oscillations. *Phys Rev A* **85**, (2012).
24. Xu, V. *et al.* Probing gravity by holding atoms for 20 seconds. *Science* **366**, 745–749 (2019).

25. Mitchell, J. T. On systematics and their mitigation in MAGIS-100 atomic interferometer experiment to explore the dark sector and early Universe. (2020).
26. Kristensen, S. L., Jaffe, M., Xu, V., Panda, C. D. & Müller, H. Raman transitions driven by phase-modulated light in a cavity atom interferometer. *Phys Rev A* **103**, (2021).
27. Storey, P. & Cohen-Tannoudji, C. The Feynman path integral approach to atomic interferometry. A tutorial. *J. Phys. II France* **4**, 1999–2027 (1994).
28. Hogan, J. M., Johnson, D. M. S. & Kasevich, M. A. Light-pulse atom interferometry. in *Proceedings of the International School of Physics ‘Enrico Fermi’* vol. 168 411–447 (2009).
29. Lerner, L. A demonstration of decoherence for beginners. *Am J Phys* **85**, 870–872 (2017).
30. Overstreet, C., Asenbaum, P., Curti, J., Kim, M. & Kasevich, M. A. Observation of a gravitational Aharonov-Bohm effect. *Science* **375**, 226–229 (2022).
31. Cristian D. Panda, Matt Tao, James Egelhoff, Miguel Ceja, Victoria Xu, Holger Müller. (2022). Quantum metrology by one-minute interrogation of a coherent atomic spatial superposition. <https://doi.org/10.5281/zenodo.7187202>.

Acknowledgments: We thank J. Axelrod, A. Reynoso, for experimental assistance; J. Lopez for technical support; L. Clark, D. Carney, N. Gaaloul, M. Jaffe, P. Haslinger, Z. Pagel, G. Premawardhana, J. Roth, A. Singh, J. Taylor for valuable discussions.

Funding: This material is based on work supported by the

National Science Foundation grants 1708160 and 2208029 (HM)

Department of Defense Office of Naval Research grant N00014-20-1-2656 (HM)

Jet Propulsion Laboratory (JPL) grants 1659506 and 1669913 (HM)

Author contributions: CDP, JE and MT built the apparatus, collected measurements and analyzed data. VX contributed to building the apparatus and initial investigations into the source of decoherence. CDP and HM wrote the original draft. HM conceptualized and supervised the experiment. All authors contributed to the review and editing of the manuscript.

Competing interests: Authors declare that they have no competing interests.

Data and materials availability: All data presented in this paper are deposited online³¹.

Methods

Atom sample preparation and detection

To describe the experiment in detail, we define a coordinate system in which \hat{z} points upwards and is aligned to Earth's gravity. The optical cavity axis is approximately aligned with \hat{z} . We define \hat{x} to lie in the horizontal plane, aligned with the direction of the MOT magnetic field coils, such that $\hat{y} = \hat{z} \times \hat{x}$ is approximately along the direction of the camera (Fig. 1a).

Initial trapping of the atoms in a 2-dimensional MOT (2D MOT) takes place in a glass vacuum chamber (not shown in Fig. 1a) which contains Cs vapor at room temperature. Four laser beams, 12.8 MHz red-detuned from the $F=4$ to $F'=5$ line in the Cs D2 manifold and the magnetic field generated by four coils create a 2D MOT. The 2D MOT axis is aligned with a differential pumping aperture tube that connects to the primary experimental chamber (octagon in Fig. 1a). The primary chamber is evacuated with ion pumps and titanium sublimation pumps to a pressure of 6×10^{-11} torr. The Cs atoms are loaded (loading time 700 ms) into a 3D MOT formed by 6 independent laser beams (wavelength 852 nm, 12.8 MHz red detuned from the $F=4$ to $F'=5$ line) with a beam diameter of ~ 3 cm and a magnetic quadrupole field. Three additional Helmholtz coils are used to zero the environmental magnetic field along the \hat{x} , \hat{y} and \hat{z} directions. The MOT atoms load at the spatial location where net environmental plus applied magnetic field is 0.

After the 3D MOT stage, the magnetic quadrupole field is turned off and the atoms are laser cooled by optical molasses to 10 μ K. The atoms are then Raman Sideband Cooled (RSC) in a 3D optical lattice (trap depth $\sim 50 E_r$, wavelength 852 nm, ~ 50 GHz red-detuned from D2), where two of the laser beams are derived from the TEM00 cavity mode and the other two are provided through the side window. The resulting RSC temperature is 0.3 μ K, near the Cs recoil limit.

The atoms are then transferred into a far off resonant 1D lattice formed by the TEM00 mode of the optical cavity (trap depth $\sim 70 E_r$, wavelength 943 nm). RSC leaves atoms in the $F = 3, m_F = 3$ stretched state¹. The atoms are then transferred using microwave rapid adiabatic passage (9 ms ramp) followed by a microwave π -pulse to the magnetically insensitive $F = 3, m_F = 0$ state.

To launch the atoms vertically upwards, the atoms are transferred into a vertically oriented lattice formed by two laser beams that enter the experiment diagonally, along the direction of the MOT laser beams. The frequency of one of the laser beams is swept to launch $\sim 80\%$ of the atoms upwards into free fall. The launch velocity is typically set to 196 mm/s, such that the atoms reach the apex of their trajectory after 20 ms of free-fall time, corresponding to a launch height of 1.96 mm. A Doppler sensitive Raman π -pulse along \hat{z} (Gaussian time profile with $1\sigma=20 \mu$ s) restricts the longitudinal atomic velocity to $v_{\parallel} = 0.6 v_r$ (Gaussian 1σ), corresponding to a temperature of 80 nK and $2\pi \cdot 8$ kHz (Gaussian 1σ) Doppler shift.

To obtain a pure sample, atoms that did not take part in the population transfer need to be removed. This is accomplished by a laser beam resonant with the D2 line (either $F = 4$ to $F' = 5$ or $F = 3$ to $F' = 2$) which travels approximately along the $-\hat{x} + \hat{z}$ direction and is used to push atoms with internal state that is either $F = 4$ or $F = 3$, respectively. It is also used at the beginning of the interferometer to push away two of the interferometer arms that are transferred in the unwanted momentum and hyperfine state (Fig. 1b).

For detection after the interferometer sequence, this same laser is used to push the atoms in $F = 4$ over a distance of ~ 1 mm relative to the $F = 3$ atoms, so that the two populations can be separately detected by fluorescence within one camera image. Fluorescence is excited using the MOT laser beams, blocking the ones along the \hat{x} direction to reduce stray light. The detection

light is typically 5.6 MHz red-detuned from the $F = 4$ to $F' = 5$ line and the atoms are imaged for 4-10 ms before imperfections in the laser light intensity profile or power imbalance push away the atom sample. This scheme measures both interferometer outputs simultaneously on the same image, minimizing detection noise due to fluctuations in the intensity or detuning of the detection light or variations in background stray light.

The camera is placed at a 45° angle with respect to the horizontal, along the $\hat{z} + \hat{x}$ direction and is pointed towards the atomic cloud. A high-NA objective (f/0.95 aperture, Navitar MVL50HS) is used to collect and image the fluorescence on the surface of the EMCCD sensor. The EMCCD gain is typically set to 0, except for long hold time measurements ($\tau > 20$ s), where the EMCCD gain is set to values up to 300x to image lower numbers of atoms ($N < 1000$).

Optical cavity and lattice imperfections

The optical Fabry-Perot cavity is formed by two curved mirrors (20 m radii of curvature) that are separated by $L = 37.5$ cm. This results in a cavity waist size of $w_0 = 760 \mu\text{m}$ and a Rayleigh length of $z_R = 1.92$ m at the lattice wavelength $\lambda_{\text{latt}} = 943$ nm. The cavity waist is located near the center of the atom cloud, which ensures that the diameter of the lattice at the top and bottom interferometer arms is as similar as possible. This minimizes dephasing due to variations in the transverse diameter of the trap potential between the top and bottom interferometer arms. Numerical simulations suggest that contrast decay due to the remaining small potential difference is now at least three orders of magnitude lower, therefore negligible at current sensitivity.

The mirror substrates are 1 inch diameter and superpolished to a root-mean square (rms) surface roughness of $< 1 \text{ \AA}$. They are dielectric coated for 97.0 % reflectivity at $\lambda_{\text{Raman}} = 852$ nm, 98.3 % at $\lambda_{\text{latt}} = 943$ nm and 93.5 % at $\lambda_{\text{tracer}} = 780$ nm. The linewidth of the cavity is 2.2 MHz at 943 nm, providing ~ 59 times power enhancement of the coupled light. The transverse mode spacing is 20 MHz, sufficiently large compared to the cavity linewidth so that most of the incoming light is coupled into a single transverse cavity optical mode.

Laser frequency stabilization scheme

A reference laser is frequency-stabilized to the Cs D2 line in a vapor cell². All the other frequency stabilization schemes described below use Pound-Drever-Hall (PDH), where the sidebands are provided by an electro-optical modulator (EOM - typical modulation frequency ~ 20 MHz). The length of a transfer cavity is stabilized with a piezo to the reference laser. The Raman laser ($\lambda_{\text{Raman}} = 852$ nm) and tracer laser ($\lambda_{\text{tracer}} = 780$ nm) are referenced to this transfer cavity. Both lasers enter the experiment science cavity from the bottom (along $+\hat{z}$), where a set of dichroic mirrors allow their reflection and transmission to be separately monitored by photodetectors. The length of the experiment science cavity described above is stabilized to the tracer laser against vibrations and slow drift due to mechanical expansion of the vacuum chamber.

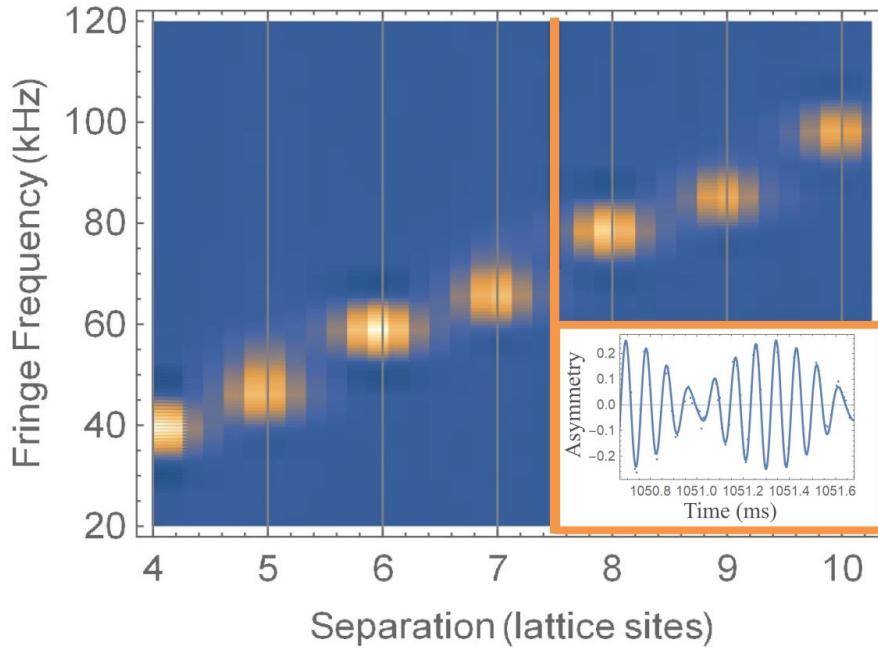
Light from the lattice laser ($\lambda_{\text{latt}} = 943$ nm) is split into two paths. A small fraction (100 μW) enters the “science” cavity through the top mirror (along $-\hat{z}$) and is used to stabilize the lattice laser to the length of the “science” cavity. The remaining light is amplified by a tapered amplifier and enters the cavity from the bottom mirror (along $+\hat{z}$). The intra-cavity power is monitored by a photodetector placed at the transmission port and is used to stabilize the intra-cavity intensity by adjusting the RF voltage amplitude driving an acousto-optic modulator (AOM). The trap depths quoted throughout the paper are calculated by scaling the measured power of this photodetector.

Lattice properties and loading

The lattice laser used in these experiments is $\lambda_{\text{latt}} = 943$ nm, 49 nm red-detuned from the D1 transition and 91 nm red-detuned from the D2 transition. Compared to our previous work, where $\lambda_{\text{latt}} = 866$ nm with single photon scattering lifetime of $2\pi/\Gamma_{sp} = 2\pi \cdot 11$ s, this larger detuning reduces decoherence to $2\pi/\Gamma_{sp} = 2\pi \cdot 120$ s for $U_{\text{latt}}^0 = 5 E_r$. This level is negligible for all measurements described here.

Near the apex of the atoms' free-fall trajectories, the optical lattice is turned on or off using a smooth exponential curve with time constant of $400 \mu\text{s}$. This is fast compared to the transverse motion of the atoms (characteristic harmonic frequency $\omega_{\perp} = 2\pi \cdot 2.4$ Hz for $U_{\text{latt}}^0 = 5 E_{\text{rec}}$), but slow compared to the axial motion (characteristic harmonic frequency $\omega_{\parallel} = 2\pi \cdot 8.2$ kHz for $U_{\text{latt}}^0 = 5 E_{\text{rec}}$). This means that the atoms adiabatically load axially into the high-intensity regions of the optical lattice, which enforces quantization of the atomic wavepacket positions during the hold.

To probe this structure, we measure interferometer fringes when finely changing the initial interferometer arm separation by varying T : $\Delta z = v_r T$. We then perform a Fourier decomposition of the measured fringes to determine the primary frequency components. We observe frequency components from gravitational potential differences that necessarily correspond to integer multiples of lattice sites: $\Delta z = n \cdot \lambda_{\text{latt}}/2$, where n is an integer number (Extended Data Figure 1).



Extended Data Figure 1. Atoms load into integer multiples of the lattice period. Fourier spectral decomposition components of the measured fringes as a function of separation. Yellow represents a higher power density at the specific fringe frequency. **Inset.** Raw data and fit for such a fringe, when the initial wavepacket separation equals 7.5 lattice sites. We observe that the optical lattice enacts a second beam splitter, where the partial atomic wavepacket loads evenly into adjacent lattice sites with 7 and 8 lattice site separations.

Interferometer phase and contrast

The interferometer phase is the sum of two terms: $\Delta\phi = \Delta\phi_L + \Delta\phi_{\text{prop}}$, where $\Delta\phi_L$ results from the interaction of atomic wavepacket with the Raman laser³ and $\Delta\phi_{\text{prop}}$ is the propagation phase. Each of the four applied laser pulses adds a term ϕ_i to this phase that is proportional to the atom's position. In our interferometer,

$$\Delta\phi_L = \phi_L^t - \phi_L^b = (\phi_1 - \phi_2) - (\phi_3 - \phi_4) = k_{\text{eff}}g T(T + t_{\text{apex}}), \quad (1)$$

where g is the local gravitational acceleration and indexes ϕ_L^t, ϕ_L^b denote the phase corresponding to the top and bottom arms, respectively. The total interferometer phase due to Earth's gravitational acceleration g amounts to

$$\Delta\phi = \Delta\phi_{\text{prop}} + \Delta\phi_L = \frac{m_{\text{Cs}}g\Delta z}{\hbar}\tau + k_{\text{eff}}g T(T + t_{\text{apex}}). \quad (2)$$

To scan interferometer fringes, we can vary either (a) the hold time, τ , or (b) the rate at which the Raman laser frequency is ramped so that it remains on-resonance with the atoms during free-fall, $\alpha = g * k_{\text{eff}} = 2\pi \cdot 23 \text{ kHz/ms}$ for the D2-line of cesium. Varying τ results in a fringe frequency that is given by

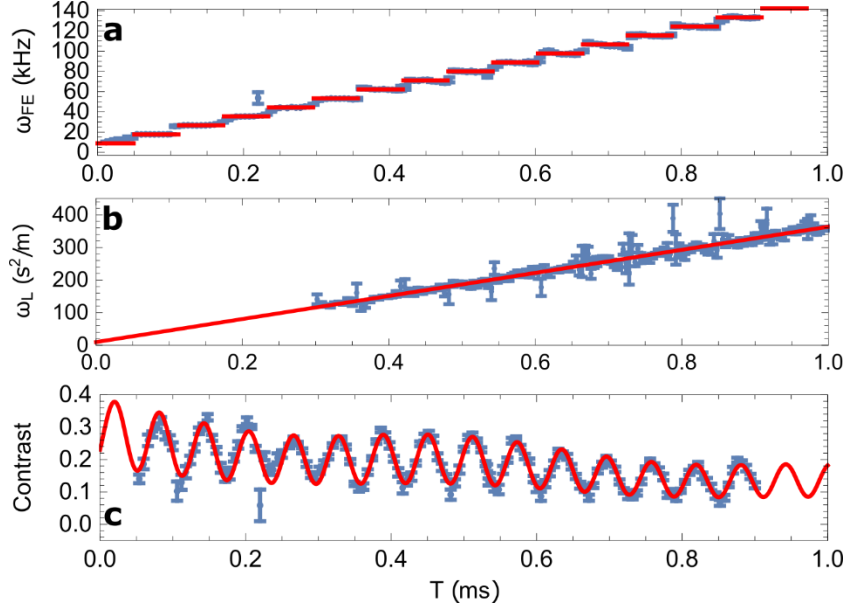
$$\omega_{\text{prop}} = \frac{\partial(\Delta\phi)}{\partial\tau} = m_{\text{Cs}}g\Delta z/\hbar. \quad (3)$$

As shown in Extended Data Figure 2a, the adiabatic loading in the optical lattice forces the wavepacket separation to be an integer number of lattice sites, $\Delta z = n \cdot \frac{\lambda_{\text{latt}}}{2}$, where n is an integer. When α is varied, the fringe frequency is

$$\omega_L = \frac{\partial(\Delta\phi)}{\partial\alpha} = k_{\text{eff}}T(T + t_{\text{apex}}). \quad (4)$$

There is no quantization of scanned parameters in this case (Extended Data Figure 2b).

The loss in fringe contrast as a function of separation is shown in Extended Data Figure 2c for a hold time of $\tau \approx 1 \text{ s}$ and is independent of whether α or τ are scanned. In addition to the slowly decaying exponential envelope discussed in detail in the main text, we also observe variation in the contrast at shorter separation length scales. The contrast varies as a function of T with a fast sinusoidal component given by lattice spacing, $\lambda_{\text{latt}}/(2v_r)$. In addition, the contrast decay curve exhibits a smaller amplitude (4% typically) sinusoidal component with periodicity given by the least common multiple of the lattice laser and tracer laser wavelengths, λ_{latt} and λ_{tracer} . This variation is due to dephasing from the interference of the lattice and tracer lasers. The separations used in Fig. 3 are chosen to minimize these additional dephasing mechanisms and only probe the slow exponential decay of contrast described in the main text. We note that this data was taken before replacing the lattice laser, so $\lambda_{\text{latt}}=866 \text{ nm}$ for data shown in Extended Data Figure 2 only.

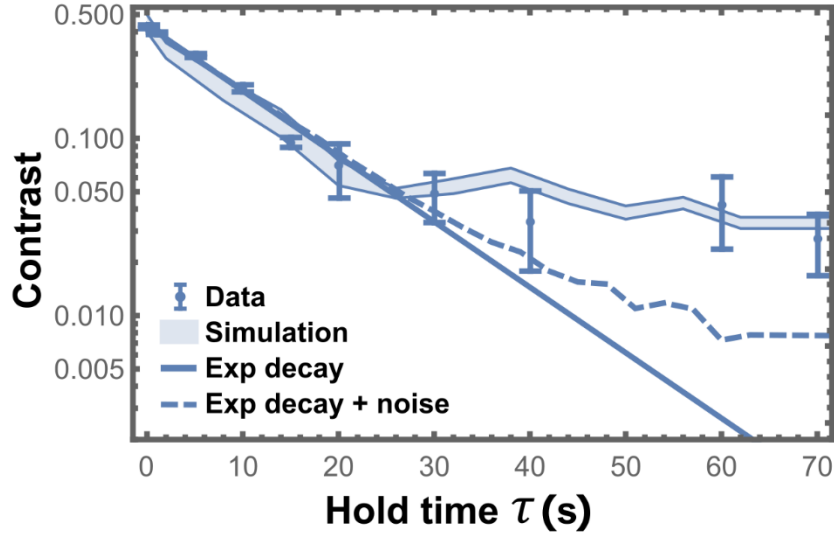


Extended Data Figure 2. Measured interferometer fringe frequency when a, the hold time τ is scanned and b, the laser ramp rate α is scanned. Blue datapoints show fitted fringe frequency as a function of separation. Error bars correspond to 1σ (68%) Gaussian confidence intervals. Red lines correspond to the expected analytical fringe frequency as shown by Eqs. 2 and 3. **c, Contrast loss as a function of separation time, T .** The fitted interferometer contrast varies as a function of T with a fast sinusoidal component given by lattice spacing, $\lambda_{\text{latt}}/2 \cdot v_{\text{rec}}$, a slowly decaying exponential envelope and a lower frequency variation due to interference of the “lattice” and “tracer” lasers. The red line fits the data using free parameters for the amplitudes of the exponential decay, amplitude of the higher frequency sinusoidal function and the amplitude of the lower frequency variation.

Contrast at long hold times

When $\tau > 20$ s, we observe a second, slower contrast decay term, $C_1 \text{Exp}(-\tau/\tau_{C1})$ ($\tau_{C1} \sim 1000$ s) (Extended Data Figure 3). Similar behavior is observed for the numerical simulations carried out in this regime. The decoherence model described in the paper suggests a slowing in the decoherence rate of our interferometer due to high energy atoms tunneling out of the interferometry trap (trap lifetime 14 s). The remaining atoms are lower energy and only sample the harmonic region of the potential, experiencing reduced decoherence. Since the C_1 term is significantly nonzero for long hold times, $\tau > 20$ s, only, we focus our analysis on the dominant contrast decay term, τ_C .

For low contrast values, noise (such as due to shot noise or imaging noise) will lead to a small bias in the contrast value extracted from the least-squares fit. We estimate this bias by fitting simulated fringes with similar levels of noise, as shown in Extended Data Figure 3. The observed slowing of the contrast decay is significantly nonzero, even when considering this small bias.



Extended Data Figure 3. Contrast loss at long hold times. Slowing down in the measured decoherence rate (points with error bars) compared to an exponential decay (solid line) when $\tau > 20$ s. The estimated bias in the measured contrast at small contrast values due to fitting data with experimental noise is shown (dashed line). This interferometer used a pulse separation $T = 0.267$ ms ($\Delta z = 1.9 \mu\text{m}$) and a peak trap depth of $U_0 = 7E_r$.

Investigating contrast loss

To find the source of decoherence, we have varied around 20 experimental parameters, looking for a dependence of the contrast decay constant κ . Most of these parameters were varied in a range that is large (factor of 2 to 1000) compared to the typical residual value in the experiment. A typical procedure involved measuring experiment fringes both under typical running conditions and when the experimental parameter was greatly exaggerated. Two fringes were taken in each configuration: one that corresponds to low Δz , U_{latt}^0 and τ , where the contrast approximately equals C_0 , and one where Δz , U_{latt}^0 and τ are set such that $C = C_0/2$, on the slope of the exponentially decaying contrast, $C = C_0 \text{Exp}[-\Delta z U_{\text{latt}}^0 \tau / \kappa]$. This makes the measurement maximally sensitive to variations in κ . Taking the ratio of the contrast values of the two fringes gives an accurate estimate of κ . The list of parameters that were investigated and found to have no influence on contrast decay is given in Extended Data Table 1.

Extended Data Table 1. Investigating the cause of contrast decay. Experimental parameters that were varied and found to have no influence on contrast decay at a level of 2%.

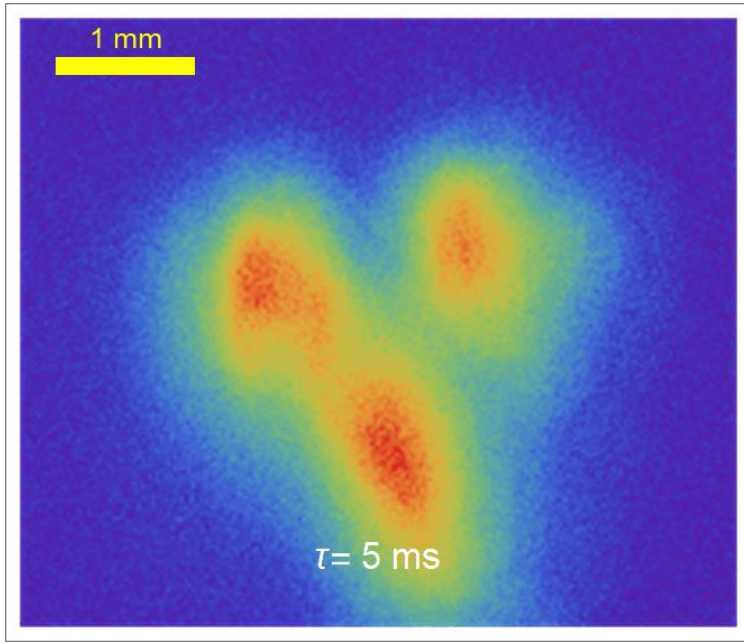
Parameter Varied	Experimental Test Performed	Observed Outcome
Radial lattice uniformity	Installed new superpolished cavity mirrors (surface rms $< 1 \text{ \AA}$)	Same κ
Axial lattice uniformity	Replaced planar- concave cavity with symmetric concave-concave cavity (mirrors have equal radii of curvature)	Same κ

Vacuum pressure	New pumps, reduced outgassing	Same κ , slower decay of atom number
Lattice laser frequency noise	2x higher with tuning PID lock	Same κ
	Narrower laser linewidth by locking to a high-finesse ($F=20,000$) cavity	
Raman beamsplitter symmetry	Symmetric beamsplitters using microwave $\frac{\pi}{2}$ pulse followed by optical π pulse (32)	Same κ
Laser lattice broadband emission	Suppressed $>10x$ with filter cavity	Same κ
Lattice intensity noise	10x reduced by intensity stabilization using transmitted light as a monitor	Same κ , slower decay of atom number
Background scatter	Increased 20x by shining mode-mismatched light at cavity mirror and/or experiment vacuum window	Same κ
Acoustic noise	Phone speaker, tapping the optical table	Same κ , vibrations primarily caused setup translation
Alignment with gravity	Tilted optical table by 1.5 mrad	Same κ , observed expected phase shift due to modified projection of local gravity along cavity axis
Changing atom number and density	2x reduction by lowering state selection efficiency	Same κ , low contrast at very low atom numbers due to increased imaging noise
Axial atom temperature selection	Reduced 3x by increasing the length of velocity selection pulse	Same κ , as expected since we only expect dependence on radial temperature
Misaligned lattice laser, coupling light to high order cavity modes	Reduced cavity coupling efficiency 2x by misaligning and changing beam diameter	Same κ
Lattice laser detuning	Replaced lattice laser with 866 nm ECDL (14 nm det.) and 1064 nm fiber laser (212 nm det.)	Same κ , except change in contrast due to single photon scattering, as expected
Environmental field gradients	Varied the vertical atom position by up to 1.5 cm	Same κ
Magnetic field gradients	Increased 1000x by turning on MOT coils during interferometer	Same κ , observed expected phase shift due to quadratic Zeeman shift
Position within the atomic sample	Analyzed horizontal and vertical slices of fluorescence image	Same κ

Loading atoms into higher order modes

Movie 1 displays a sequence of fluorescence images showing the atom cloud being loaded into the horizontally asymmetric Hermite-Gauss TEM01 mode of the optical cavity.

To produce data shown in Fig. 3 of the main text, we use higher order cylindrically symmetric Laguerre-Gauss modes (LG10, LG20), which have increasingly narrower mode diameters of the central peak. Lattice laser light is coupled into these higher order modes by increasing the diameter of the incoming laser beam such that the incoming Gaussian beam has good overlap with the LG modes (typically 20-30%). An AOM is used to sweep the lattice laser frequency (sweep time 1 ms) over the optical cavity transverse mode spacing, switching between coupling the lattice laser to the LG00 and either LG10 (20 MHz sweep) or LG20 (40 MHz sweep range).



Movie 1. Sequence of fluorescence images showing dynamics of the spherically symmetric atom cloud loading into a TEM01 mode of the optical cavity. The yellow and red colors represent regions of space with high atom density. The atoms that have good overlap with the cavity get loaded and initially oscillate (period 150 ms) before eventually (after 300-400 ms) filling the available cavity mode trap volume.

Numerical simulation

As mentioned in the main text, we use a simulation with parameters that match our knowledge of the experiment to estimate the effect of lattice imperfections on interferometer decoherence. The simulation starts with a sample of 500-1000 atoms generated with 2D positions and velocities (in the xy plane) that randomly drawn from Gaussian distributions with diameters of $540 \mu\text{m}$ and 26 mm/s , respectively. Each atom's trajectory parameters $\{x(t), y(t), v_x(t), v_y(t)\}$ are calculated by integrating the equations of motion in each x, y spatial direction

$$\frac{dx(t)}{dt} = v_x(t) \quad (5)$$

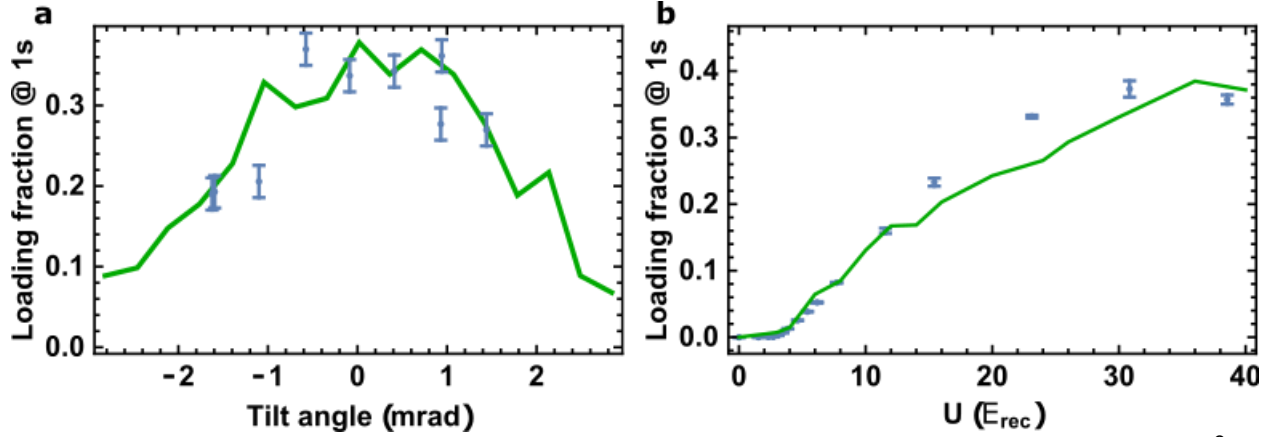
$$\begin{aligned}\frac{dy(t)}{dt} &= v_y(t) \\ \frac{dv_x(t)}{dt} &= \frac{dU_{\text{latt}}(x(t), y(t), t)}{dx} \frac{1}{m_{\text{Cs}}} \\ \frac{dv_y(t)}{dt} &= \frac{dU_{\text{latt}}(x(t), y(t), t)}{dy} \frac{1}{m_{\text{Cs}}},\end{aligned}$$

where $U_{\text{latt}}(x(t), y(t), t) = 0$ for the first 38 ms, corresponding to free-propagation and then $U_{\text{latt}}(x(t), y(t), t) = U_0 \text{Exp}\left(-\frac{(x-x_0)^2 + (y-y_0)^2}{2w^2}\right)$ during the lattice hold, where $x_0 = y_0 = 0$ for the unperturbed potential. In addition to trajectory parameters, probabilities for the atoms to leave the trap $p(t)$ are calculated from the Landau-Zener criterion⁴ through $\frac{dp}{dt} = \ln\{1 - \text{Exp}\left[-\frac{\pi}{64} \frac{a_{\text{Cs}}}{g} \frac{U_{\text{latt}}(x(t), y(t), t)}{E_r}\right]\}$, where $a_{\text{Cs}} = \frac{2\pi\hbar}{m_{\text{Cs}} g \lambda_{\text{latt}}/2}$. An atom that tunneled is assumed to have left the experiment and does not contribute to the interferometer output. The integration uses a Runge-Kutta routine, where the timestep (typically 100 μs) is much shorter than the timescales of the motion (10s of Hz). We verify that simulation results are independent of timestep size choice within an order of magnitude.

The interferometer propagation phase is calculated from $\phi_{\text{latt}}^{\text{prop}}(t) = \int \mathcal{L} dt$, where $\mathcal{L} = \frac{1}{2} m_{\text{Cs}} (v_x(t)^2 + v_y(t)^2) - U_{\text{latt}}(x(t), y(t), t)$. The trajectory parameters, $p(t)$ and $\phi_{\text{latt}}^{\text{prop}}(t)$ are each calculated for two separate configurations: (a) one interferometer arm in an unperturbed Gaussian potential and (b) one interferometer arm perturbed by imperfections of the optical lattice, such as tilts. The effect of tilts is modeled by moving the center of the lattice potential to a time-dependent position $x_0(t) = a_{\text{tilt}} \sin(\omega_{\text{tilt}} t)$, where $a_{\text{tilt}} = \theta \Delta z$ is the tilt-induced lattice amplitude change. At the end of the integration, the separation phase is calculated from the final positions and velocities as $\phi_{\text{latt}}^{\text{sep}}(t) = [(x^t - x^b)(v_x^t + v_x^b) + (y^t - y^b)(v_y^t + v_y^b)] m_{\text{Cs}} / (2\hbar)$. The total phase is then $\phi_{\text{latt}}(t) = \phi_{\text{latt}}^{\text{prop}}(t) + \phi_{\text{latt}}^{\text{sep}}(t)$.

The differential phase $\Delta\phi_{\text{latt}}$ between the top and bottom arms, is calculated by subtracting the two phases. The average ensemble phase shift $\langle \Delta\phi_{\text{latt}} \rangle$ and phase spread, $\delta(\Delta\phi_{\text{latt}})$ are calculated by performing a sum over all atomic trajectories. The effect of the phase spread $\delta(\Delta\phi_{\text{latt}})$ on the fringe contrast \mathcal{C} is quantified by computing an average of fringes with phases given by the ensemble phase distribution, each weighted by their individual Landau-Zener survival probabilities, $p(t)$. A third contribution to fringe contrast loss due to poor overlap of the atomic wavepackets at the end of the interferometer is found to be negligible compared to the dephasing described above. The contrast decay time constant $\tau_{\mathcal{C}}$ is extracted from a decaying exponential fit (where $\tau_{\mathcal{C}}$ is the only free parameter) of the fringe contrast sampled for $t = 0$ to $t = 20$ s in steps of 0.2 s. The simulation time was extended to 70 s for generating Extended Data Figure 3. We find good agreement between the simulations and experimental data (Figure 3).

We verify the performance of the trajectory simulation by measuring the lattice loading fraction under different laboratory conditions and comparing the resulting atom numbers with the simulation, as a fraction of the initially available atoms. We find good agreement between the atom numbers loaded and remaining in the lattice after a 1 second hold, when the experiment and simulation tilt is varied (Extended Data Figure 4a) and when the trap depth is varied (Extended Data Figure 4b).



Extended Data Figure 4. Loading fractions vs a, global tilt angle and b, trap depth, U_{latt}^0 . Experimental data showing fractions of atoms remaining after loading and 1 second of hold time as a function of initial number. Experimental data is shown by blue dots with error bars corresponding to 1σ (68% confidence) Gaussian intervals, and simulation results are in green.

Density matrix formalism

We use a density matrix formalism to show that a Lorentzian distribution in atom phases, $\delta(\Delta\phi_{\text{latt}})$, results in an exponential decay of the ensemble contrast²⁹, as shown in Eq. 5 of the main text. Initially, the atoms are in a coherent superposition state of the top and bottom arms: $|\psi\rangle_i = (|t\rangle + |b\rangle)/\sqrt{2}$. This corresponds to a pure state density matrix:

$$\rho_i = |\psi\rangle_i \langle \psi|_i = \frac{1}{2} \begin{pmatrix} 1 & 1 \\ 1 & 1 \end{pmatrix}. \quad (6)$$

While in the optical lattice, the lower lattice site accumulates phase $\Delta\phi_{\text{latt}}$ and the state evolves as: $|\psi\rangle_f = (|t\rangle + e^{i\Delta\phi_{\text{latt}}}|b\rangle)/\sqrt{2}$, corresponding to evolution operator $\mathcal{E}(\Delta\phi_{\text{latt}}) = \begin{pmatrix} 1 & 0 \\ 0 & e^{i\Delta\phi_{\text{latt}}} \end{pmatrix}$. The final density matrix of the two-level system is given by $\rho_f = \int_{-\infty}^{\infty} \mathcal{E}(\phi) \rho_i \mathcal{E}^\dagger(\phi) P(\phi) d\phi$, which evaluates to

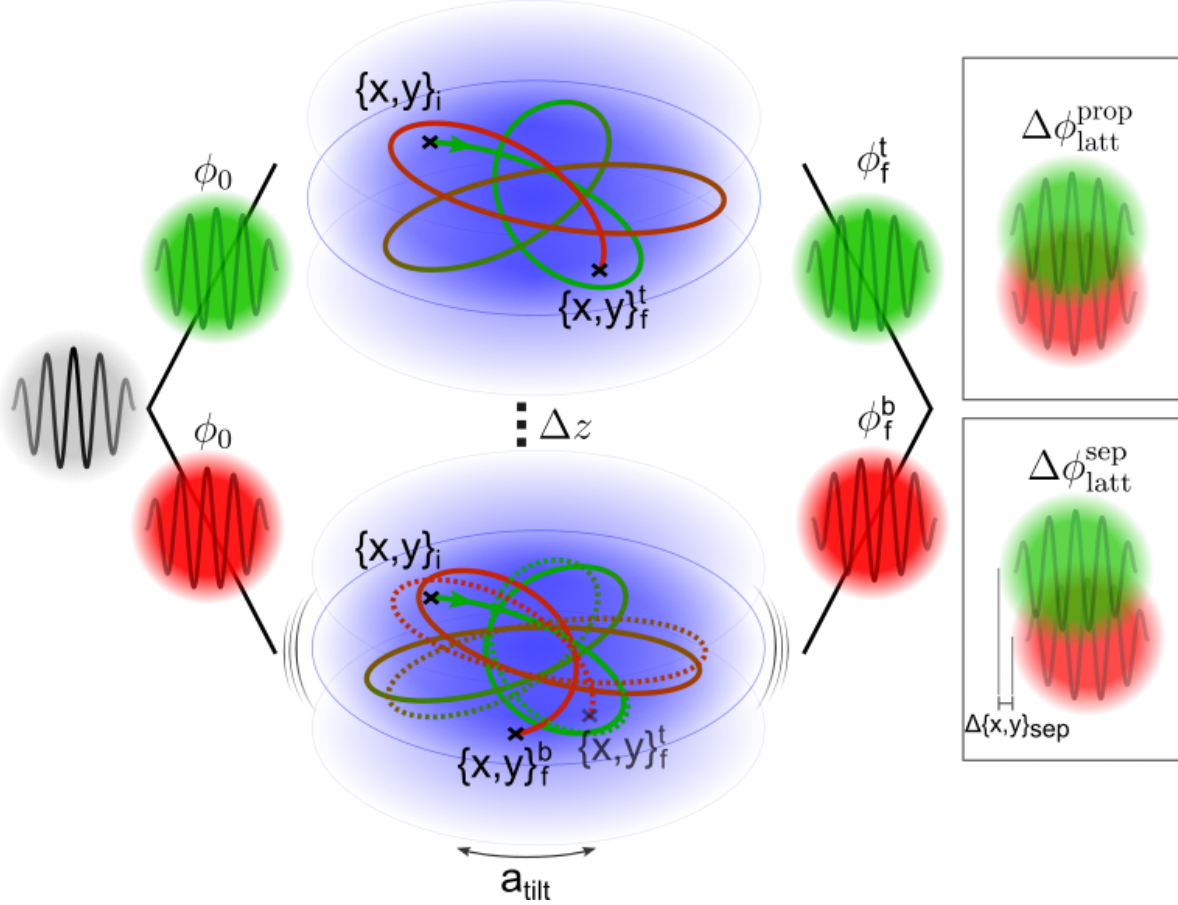
$$\rho_f = \frac{1}{2} \begin{pmatrix} 1 & \text{Exp}[-\delta(\Delta\phi_{\text{latt}})] \\ \text{Exp}[-\delta(\Delta\phi_{\text{latt}})] & 1 \end{pmatrix}. \quad (7)$$

This represents a mixed state where the off-diagonal terms describe the coherence of the system. The contrast thus tends to zero for a large phase spread

$$C = C_0 \text{Exp}[-\delta(\Delta\phi_{\text{latt}})]. \quad (8)$$

Lattice trajectories and contributions to lattice phase shift

The diagram shown in Extended Data Figure 5 is a pictorial representation of the atomic trajectories inside the optical lattice and resulting differential phase shifts between the top and bottom interferometer wavepackets due to oscillatory tilts. It complements the description of decoherence due to such effects in the main text.



Extended Data Figure 5. Phase shifts due to differential motion between the atomic wavepacket in the top (unperturbed) and bottom (perturbed) lattice sites. The atomic wavepacket (wavy line on top of grey disk) is split into an equal superposition of two partial wavepackets (wavy lines on top of green and red disks). The partial wavepackets are loaded into lattice sites (blue ovals) that are spatially separated by a distance of Δz . Solid lines show representative atom trajectories in the two lattice sites, which are both initially loaded at position $\{x, y\}_i$. Survival probabilities due to Landau-Zener tunneling are shown by the trajectories color gradients and range from 1 (green) to 0 (red). Time-dependent tilts with amplitude a_{tilt} cause the position of the lower lattice site to oscillate in the transverse plane, while the top lattice site is unperturbed, leading to a displaced trajectory of the bottom atom partial wavepacket with final position $\{x, y\}_f^t \neq \{x, y\}_f^b$ and propagation phase difference $\phi_f^t \neq \phi_f^b$. The rightmost panels show the two main dephasing mechanisms, due to differential free-evolution phase, $\Delta\phi_{\text{latt}}^{\text{prop}}$, and separation phase, $\Delta\phi_{\text{latt}}^{\text{sep}}$.

1. Treutlein, P., Chu, K. Y. & Chu, S. High-brightness atom source for atomic fountains. *Phys Rev A* **63**, 514011–514014 (2001).
2. Zi, F. *et al.* Laser frequency stabilization by combining modulation transfer and frequency modulation spectroscopy. *Appl Opt* **56**, 2649 (2017).
3. Jaffe, M., Xu, V., Haslinger, P., Müller, H. & Hamilton, P. Efficient Adiabatic Spin-Dependent Kicks in an Atom Interferometer. *Phys Rev Lett* **121**, (2018).

4. Cladé, P. Bloch oscillations in atom interferometry. *arXiv:1405.2770v1* (2014)
doi:10.1393/ncr/i2015-10111-3.